

Dear reviewer #1,

Thank you for your comments and suggestions regarding our manuscript. Listed below are our itemized responses, with the original comment/question displayed in italics.

- 5 1. *Page 2, Line 9: Several references to column water vapor are made throughout the paper, this being the first one. Although the surface echo (or cloud for ground based measurements) may be exploited to directly measure the column water vapor, no discussion is presented on the challenges associated with this measurement, specifically, to what accuracy the differential power ratio between the different sounding frequencies need to be measured. Back of the envelope calculations show a relative error of 10^{-4} is required in the relative transmitted power ratio, which is certainly a difficult task. A brief discussion (somewhere in the paper) on the column measurement requirements would be beneficial.*

10 Indeed, we mention multiple times the capability of an airborne (or spaceborne) version of this instrument to measure the total water column using surface returns. However, this is not a focus of this paper, which is concerned with profiling within boundary-layer clouds. Thus, we do not deem it appropriate to discuss the technical or systematic details pertaining to such a measurement.

- 15 Furthermore, it is not clear how the reviewer arrived at their back of the envelope calculation. If the gas extinction cross section $\kappa(f)$ doesn't change appreciably in the part of the atmosphere where the majority of water vapor resides, the total column water vapor (TCWV) for surface returns from two frequencies is

$$\text{TCWV} = \frac{1}{2\Delta\kappa} \left[\ln \left(\frac{P_e(R_s, f_1)}{P_e(R_s, f_2)} \right) + \ln \left(\frac{C(f_2)}{C(f_1)} \right) + \ln \left(\frac{\sigma_0(f_2)}{\sigma_0(f_1)} \right) \right]. \quad (1)$$

- 20 Here $\sigma_0(f)$ is the surface cross section, R_s is the distance to the surface, $[\text{TCWV}] = \text{kg/m}^2$, and all other variables are as in the manuscript. The uncertainty from the first term on the right hand side corresponds to radar speckle, and thus decreases (in relative error) as the square root of the number of pulses. The main systematic concern, therefore, is the second term, related to radar calibration. Defining $\alpha = C(f_2)/C(f_1)$, the relative error in the retrieved value is therefore

$$\frac{\sigma_{\text{TCWV}}}{\text{TCWV}} = \frac{1}{2\tau} \frac{\delta\alpha}{\alpha}. \quad (2)$$

- 25 So, if we have an average of 5 g/m^3 of water vapor in the lowest 5 km of the atmosphere, we already have $\tau = 1.5$ for $f_1 = 167 \text{ GHz}$ and $f_2 = 174.8 \text{ GHz}$. Thus, a 5% relative error in the retrieved TCWV corresponds to an error in α of 15%. This is a significantly less demanding level of accuracy than that proposed by the reviewer. An identical argument holds for uncertainties in the differential surface cross section.

- 30 2. *Page 3, Line 1: Please clarify that the column measurements do require absolute calibration.*

As is evident from the above analysis, absolute calibration of the radar system is **not** required, but rather only relative calibration at the two frequencies. For the same reasons discussed above, we don't feel this information should be included in the main paper, since no total column measurements are discussed.

- 35 3. *Page 3, Line 4: An assumption is made that the effects of multiple scattering are negligible on the received echo within clouds. This subject is not mentioned again in the paper. It is unclear that this assumption is valid and is highly dependent on the cloud water and ice particle size distributions. At the optical frequencies, lack of quantitative knowledge of the multiple scattering limits the utility of the received signal within clouds. The effects of multiple scattering become significantly larger as the beam propagates deeper into the cloud. This effect has been quantified at the microwave frequencies such as Cloud Sat and should be more completely addressed in this paper. A discussion on the impacts of multiple scattering on the humidity retrievals for different cloud particle size distributions and viewing geometries (distance to scattering target (ground vs airborne vs space) should be presented.*

40 While multiple scattering effects are a primary concern of any spaceborne millimeter-wave radar, we disagree that discussion of multiple scattering need be a prominent part of the paper, which focuses on near-range ground based

testing. However, for completeness in this response we provide a brief quantitative treatment of when this could become a problem. The degree of multiple scattering within a cloudy volume depends on the ratio $\chi = X/\ell_t$, where X is the radar beam footprint at the range of interest and $\ell_t = \beta_s^{-1}(1 - \tilde{\omega}g)^{-1}$ is the *transport* mean free path, which is different from the scattering mean free path $\ell_s = \beta_s^{-1}$ (see R. Hogan, *J. Atmos. Sci.*, 65, 2008). Here β_s , $\tilde{\omega}$, and g are the scattering coefficient, single-scattering albedo, and asymmetry parameter, respectively, integrated over the drop size distribution (DSD). Multiple scattering effects become important when χ is of order unity or larger.

The first attached figure shows the dependence of χ on the characteristic drop diameter of a DSD for clouds and rain at a range of 1 km. The system utilizes a 6 cm primary aperture with a 10 dB taper, corresponding to a far-field 3 dB antenna full width of 1.9 degrees. The scattering parameters are integrated over a modified gamma distribution of the form

$$N(D) = \frac{N_0}{\Gamma(\nu)D_n} \left(\frac{D}{D_n}\right)^{\nu-1} e^{-D/D_n}, \quad (3)$$

where N_0 is the peak number concentration, D_n is the characteristic diameter, and ν is the shape parameter. Here, we use $\nu = 1$ for rain and 4 for cloud. Furthermore, we implement a parametrization of N_0 as a function of D_n , which has been shown to better match observations than e.g. Marshall-Palmer (see Abel and Boutle, Q. J. R. Meteorol. Soc., 2012). This parametrization determines the rain rate for a given D_n . For clouds, we fix the liquid water content (LWC) to 1 g/m³. Clearly, from the figure we see that multiple scattering is not an issue (i.e. $\chi \ll 1$) for the measurements presented in this work.

To determine when multiple scattering is an issue from a spaceborne platform, it is necessary to use a more realistic antenna size for such a system. Accordingly, the second figure attached shows that same plot for a 1 meter aperture and 10 dB taper, this time for a range of 400 km. In this case, we see that there is a range of diameters for which χ is of order unity. Furthermore, one can simply scale the values of χ for clouds linearly to consider LWC values different than 1 g/m³. Multiple scattering will thus be an important consideration from a spaceborne platform. However, the modest values of χ mean that the effects are not so deleterious as to render information retrieval impossible, as in the case of in-cloud lidar measurements.

4. *Page 4, Lines 11-13. It should be noted that comparison on sensitivity between pulsed and FMCW is dependent on background signal levels. In high background levels with the FMCW IF bandwidth compared to the background within the gate width of a pulsed system, the advantage quickly diminishes.*

We do not understand the reviewer's point here, and ask them to clarify if our explanation here doesn't suffice. In short, the background signal level, specifically meaning noise power P_n within a single range bin, is only a function of noise temperature T_n and integration time τ , with $P_n = k_B T_n / \tau$. For all classes of radar, the signal-to-noise ratio is given by $SNR = P_e \tau / k_B T_n$, where τ corresponds to the pulse width. Of course, for conventional pulsed radar, one must use very short pulses to achieve reasonable range resolution (e.g. $\tau = 3.3 \mu s$ for CloudSat), while for chirped-pulsed and FMCW radar, ranging is related to the chirp bandwidth, not pulse duration. Thus, using the CloudSat pulse repetition frequency of roughly 4 kHz, one can achieve the same sensitivity using an FMCW system with $3.3 \mu s \times 4 \text{ kHz} \approx 1\%$ of the transmit power.

5. *Page 5, Line 10. The advantage of selecting such a high chirp frequency (60 MHz) is not clear, especially when the DAR retrievals are done over an equivalent bandwidth of $\approx 2-3 \text{ MHz}$. Please clarify on why the higher chirp frequency was selected.*

The choice of chirp bandwidth involves a compromise between acquiring more statistically independent measurements (i.e. larger chirp bandwidth) within a given volume, which is advantageous for high-SNR targets where uncertainty is limited by radar speckle, and averaging down the noise within that same volume (i.e. smaller chirp bandwidth) for low-SNR targets. In this work, we chose to purposefully oversample the range dimension with a radar resolution of 2.5 meters in order to achieve low power measurement uncertainty for our desired profile resolution of 27.5 meters. A sentence has been added in the text to clarify this point.

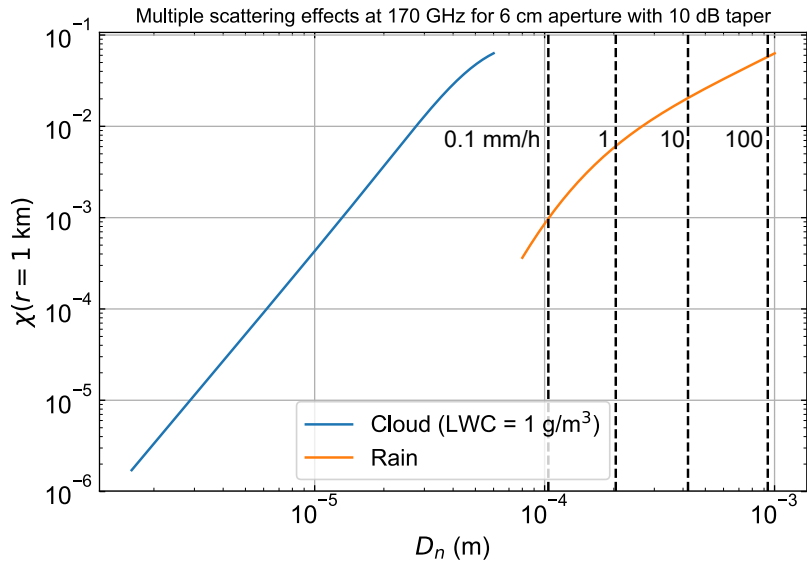


Figure 1. Multiple scattering parameter $\chi = X/\ell_t$ for cloud and rain at a range of 1 km using a 6 cm primary aperture, using the drop size distributions discussed in the revised version of the manuscript. For clouds, we use a fixed liquid water content (LWC) of 1 g/m^3 . For rain, the only free parameter is the characteristic diameter (see manuscript). Vertical dashed lines and associated labels correspond to the rain rate values at that diameter.

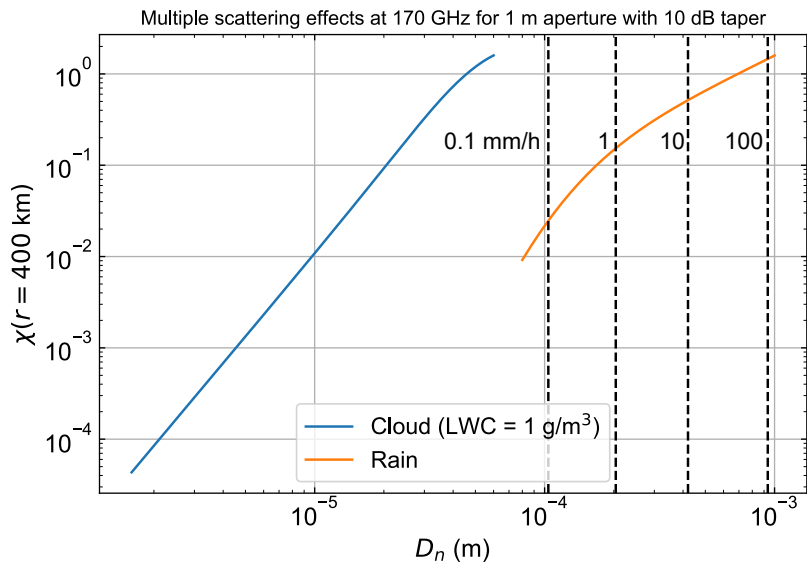


Figure 2. Same as figure 1, except for the case of a spaceborne G-band radar with a 1 meter primary aperture and a range of 400 km.

6. Page 5, Line 16. A linear chirp results in side lobes in the power spectra which can contaminate the signal from the main lobe. Please discuss the logic behind choosing a linear chirp instead of a non-linear chirp such as one with a Gaussian frequency distribution which would result in a Gaussian response in the time domain. A plot showing the power spectra (and resulting side lobes) from a bright scatterer would be beneficial to the reader.

In short, the linear chirp is not responsible for side lobes. Side lobes in the range dimension for FMCW and chirped-pulsed radar result from the Fourier transform of the finite duration pulse. Indeed, we do limit side lobes during our digital signal processing step by applying a Hanning window to the time-domain signal before taking an FFT. See page 5 line 14 of the original manuscript. As is well known, application of a Hanning window reduces the first (and strongest) side lobe to -32 dB below the main lobe, thus removing any concern that side lobe effects contaminate adjacent radar signals.

7. *Page 5, Figure 2. Update the figure to accurately represent the bi-directional chirp discussed in the text.*

The figure has been updated to show both directions of the chirp.

8. *A single table describing the system parameters would be good in section 2.2. Of particular interest is the antenna beam width and spatial side lobes.*

We have added important properties of the beam profile into a new table in section 2.2.

9. *Page 8, First paragraph. Please clarify why background subtraction is done in the Fourier domain and not in the time domain.*

It is impossible to subtract Gaussian white noise in the time domain; it is the noise *power* which must be subtracted (related to the variance of the white noise in the time domain). This is done using the power spectral density in Fourier space. To see this, we consider the downconverted radar signal in the intermediate frequency (IF) band resulting from a single target volume of distributed scatterers at range r_0 . The time domain signal is of the form $s_d(t) = s_e(t) + s_n(t) = A_e \cos(2\pi f_{IF}(r_0)t + \phi_e) + s_n(t)$. Here A_e is the peak signal voltage corresponding to the target echo and $s_n(t)$ represents white noise, which is a random variable with zero mean, and is uncorrelated in time (i.e. $\langle s_n(t_1)s_n(t_2) \rangle \propto \delta(t_1 - t_2)$). Since the noise signal voltage at a given IF frequency originates from a large number of uncorrelated sources, the statistics of each Fourier component of $s_n(t)$ are identical to those within the Rayleigh fading model (i.e. speckle statistics). Clearly we can't subtract $s_n(t)$ in the time-domain signal above, since it is impossible to *simultaneously* measure s_d and s_n . Furthermore, since the term of interest to us (the echo voltage term) contains a randomly fluctuating phase (ϕ_e) from pulse to pulse, we can only measure the variance of the echo voltage amplitude (i.e. the power), as the mean value vanishes. For these reasons, one works with radar signals in the form of power spectral densities.

Dear reviewer #2,

Thank you for your comments and suggestions regarding our manuscript. Listed below are our itemized responses, with the original comment/question displayed in italics.

- 5 1. *In The statement at line 7 and 8 in the abstract you should clearly state that this is obtained in conditions of high SNR. Also it is driven by the range of your frequency within the absorption line, this should be mentioned otherwise the reader may generalize this conclusion erroneously.*

The abstract has been updated to provide this clarification regarding the quoted water vapor uncertainty.

- 10 2. *Line 14 page 2: the authors should mention the obvious caveat of attenuation in reducing the SNR (too much water content/rain drives the signal below sensitivity).*

A sentence has been added to clarify that increased reflectivity due to increased cloud water content has an associated increase in attenuation.

- 15 3. *Line 4 page 3: it would be beneficial to discuss when the assumption of negligible multiple scattering is negligible or refer to previous literature.*

Please see our detailed response to reviewer #1 on this same point.

- 20 4. *Line 4-7 page 4: I am not fully convinced by this maximum differential absorption from particulate extinction of 0.01 dB/km. I haven't tried a specific computation but liquid cloud extinction is proportional to $1/\lambda$. So (assuming that the changes in refractive indices are negligible) a change of roughly 3% in lambda should correspond to a change of 38 dB/km/(g/m³), which means that a deep cumulus cloud with 3 g/m³ could produce 0.08 dB/km (an order of magnitude larger than quoted).*

The issue of differential absorption from hydrometeors is an important one. We have added an extended discussion to the manuscript with Mie calculations for a wide range of realistic cloud and precipitation scenarios.

- 25 5. *Line 10 page 5: What is the rationale for using a ΔF_{chirp} of 60 MHz and thus a range resolution of 2.5 m (with the obvious need of averaging later on for improving the SNR?)? Why not using a smaller bandwidth in first place?*

Please see our response to reviewer #1, item #5.

- 30 6. *Line 11-12 page 7: I do not see the need of dropping the v subscript on κ , I would recommend to keep it for clarity (otherwise the reader may think it is the total extinction).*

We have inserted the subscript v on κ throughout the manuscript.

- 35 7. *Generally in literature SNR values are stated in dB. In Fig.4 and its discussion you use linear units. Fig6 is also confusing to me, why using an obscure value like eta in the x-axis instead of using the SNR itself?*

We have modified figures 3 and 4 and the associated discussion to express SNR in dB. While the quantity η may seem obscure, we feel it is necessary to combine the uncertainty of all the power measurements involved in the humidity extraction for the purposes of the analysis in this section. Since there are N_f different power measurements from 2 different ranges involved, all with different SNR values, the humidity extraction cannot simply be labeled by a single SNR. Due to the confusion caused by this figure, we have decided to remove it from the manuscript.

8. *Fig5: it could help the reader to have a double y axis with the plot of the relative humidity and its uncertainty as well.*

Since we do not have measurements of the coincident temperature field, we do not feel it is appropriate to report relative humidity values and errors.

9. *Fig5: A couple of points at low and far ranges from the two independent datasets in the bottom right panel seem to disagree, any comment?*

One shouldn't expect independent sample sets of the same random variable to always have error bars overlapping, as this would signify an overestimate of the distribution variance. The error bars appear representative of the variability between data sets.

5

10. *Fig 6: apart from the selection of the x-axis I struggle in extracting information from this figure. Why not doing a contour plot of σ_ρ/ρ using SNR vs rho e.g. for 100 200 and 400m integration? Anyhow I would ask the authors to try to rethink the figure and present it in a more understandable way.*

We have decided to remove this figure from the manuscript, as well as section 4. Instead, we briefly discuss the trade-off between humidity measurement precision and resolution at the end of section 3.

10

Dear Professor Mace,

Thank you for your comments and suggestions regarding our manuscript. Listed below are our itemized responses, with the original comment/question displayed in italics.

- 5 1. *At what point will multiple scattering become a limiting factor? At these high frequencies and the typical optical depths of shallow cumulus - perhaps with coexisting precipitation - it seems that multiple scattering may be an issue.*

Please see our detailed response to reviewer #1 on this same point.

- 10 2. *Will the accuracy be sufficient to measure realistic supersaturations in cumulus updrafts? It seems that from a science perspective such knowledge is key. Then combining this instrument with more traditional radars and lidars, one could examine aerosol cloud interaction problems by knowing the cloud droplet number concentration and humidity near cloud base where aerosol populations become activated. Additional science applications could examining the entrainment processes near cloud top where dry tropospheric air is mixed into the marine boundary layer. It seems as though the accuracy required for these topics might push the limitations of the technology.*

15 These questions regarding the impact of DAR humidity measurement accuracy on science applications are very important, and will be the subject of future focused study after performing validation measurements with coincident measurements from radiosondes, water vapor DIALs, etc. We will provide some useful numbers here which will lay out the expected *precision* of our system, but must leave the *accuracy* discussion for future work. The relative error in the DAR humidity measurement for a two-frequency system in the high-SNR regime is given by $\sigma_\rho/\rho = \xi(N_b)/(\Delta\tau\sqrt{N_p N_b})$, where all of these parameters are defined in the manuscript. As a specific example, we imagine measuring convective updrafts from a ground-based platform, and allow the DAR system to measure for 1 minute. In this case, for 2 transmit frequencies and 1 ms pulse duration, we acquire $N_p = 3 \times 10^4$ pulses, and then use the same downsampling that is used in the paper, $N_b = 11$. For typical boundary-layer parameters, the differential absorption cross section between 174.8 and 167 GHz is $\Delta\kappa = 0.06 \text{ km}^{-1}/(\text{g/m}^3)$. Therefore, using the same retrieval step size as in the paper $R = 200 \text{ m}$, we find a humidity precision of

25
$$\frac{\sigma_\rho}{\rho} = 0.19 \times \frac{1 \text{ g/m}^3}{\rho}. \quad (4)$$

If we're observing a level within the updraft with a temperature of 20 °C, the corresponding saturated water vapor density is 17 g/m³. Thus, for 10% supersaturation we would have a measurement precision of 1%. At 0 °C, the saturated density is 5 g/m³, making the expected precision 4%. These calculations show that it is possible to achieve the necessary precision to measure large supersaturations (10-20%) in intense updrafts. Such supersaturation values are predicted in models that include prognostic supersaturation, but have yet to be observed. However, for ordinary convection, including shallow convection, where supersaturation does not typically exceed 1%, a DAR measurement confirming supersaturation would not be possible. Additional considerations for such a measurement include the necessary retrieval resolution and the timescale over which an initially supersaturated volume becomes one with RH ≤ 100 (e.g. from advection).

30 Additionally, it is important to point out that with more freedom to transmit in other frequency bands near the 183 GHz line, the retrieval resolution and precision can be substantially reduced. It is easy to find a pair of frequencies for which $\Delta\kappa$ is an order of magnitude larger or more. If such frequencies were used, one can use that factor of 10 increase in sensitivity to reduce the step size R , the humidity precision, or a combination of both.

35 It is not exactly clear to us what is meant by the final sentence as it pertains to dry-air entrainment near cloud tops. As an example measurement for this phenomenon, imagine an airborne DAR flying just above the marine boundary layer. From the first radar echos (in range) one can measure the short water column between the aircraft and the cloud top. Then, the in-cloud humidity profile can be retrieved using the subsequent radar returns from throughout the cloud volume. We would expect the dry-air entrainment signature to be a sharp gradient of the water vapor density collocated with the cloud top inferred from the reflectivity profile. With the current DAR system (i.e. in the 167 to 174.8 GHz band), the retrieval resolution is too coarse to resolve this mixing process at the top of the stratocumulus layer, which has a spatial scale on

the order of 10 meters. As mentioned in the previous paragraph, a DAR operating closer to the line center achieves much higher spatial resolution, and could potentially resolve this effect.

3. *For the topics identified in point 2, validation with radiosondes would be inadequate. Would current in situ technology for measuring water vapor allow for validation of the technique?*

5 4. We're not quite certain what is intended by this comment and question. In general, our validation approach will be to utilize radiosonde measurements in scenarios where they measure RH and T very accurately, and compare this with the DAR measurements. Note that in typical cloud scenarios, $RH \approx 100\%$ and is measured well by radiosondes, with the resolution, precision and accuracy exceeding that expected for the DAR. Since there is nothing fundamentally different from a millimeter-wave scattering perspective between the proposed validation scenario and those referenced in point 2,
10 we see no need for improved validation data.

The following is a list of all relevant changes made to the manuscript:

1. Added a sentence in the abstract clarifying that the humidity error of 0.6 g/m^3 corresponds to the high-SNR limit, and that this value is specific to the frequency band used in the measurement. (reviewer #2, item #1)
- 5 2. We removed part of the final sentence of the abstract discussing the analysis in Fig. 6 of the original manuscript. This analysis was removed in the new version of the manuscript. (reviewer #2, items #7 and #10)
3. Added a paragraph to the introduction section highlighting the novelty of our system as a G-band atmospheric radar, and giving some background on how G-band radars in general can benefit the atmospheric remote sensing community.
4. Put the v subscript on all absorption cross sections κ to clarify that these refers to water vapor absorption. (reviewer #2, item #6)
- 10 5. Added an extended discussion on differential particulate extinction for both liquid cloud droplets and precipitation, including a new figure (Fig. 2 in revised manuscript). (reviewer #2, item #4)
6. Updated figure on FMCW radar (Fig 3 in revised manuscript) to show both directions of the chirp. (reviewer #1, item #7)
- 15 7. In section 2.2, paragraph 2, added discussion on factors influencing the choice of chirp bandwidth, and therefore radar range resolution. (reviewer #1, item #5 and reviewer #2, item #5)
8. Added table in section 2.2 with all of the relevant radar hardware and signal acquisition parameters. (reviewer #1, item #8)
9. Changed all reported SNR values (including in plots in Fig 4 and Fig B1) to be expressed in dB. (reviewer #2, item #7)
- 20 10. Removed section 4 from the original manuscript, and moved short discussion of trade-off between retrieval resolution and precision to the end of section 3.2. (reviewer #2, items #7 and #10)
11. Changed colors of traces in Fig B1 so that they are more distinguishable.

Boundary-layer water vapor profiling using differential absorption radar

Richard J. Roy, Matthew Lebsock, Luis Millán, Robert Dengler, Raquel Rodriguez Monje, Jose V. Siles, and Ken B. Cooper

Jet Propulsion Laboratory, California Institute of Technology, Pasadena, California, USA

Correspondence: Richard J. Roy (richard.j.roy@jpl.nasa.gov)

Abstract. Remote sensing of water vapor in the presence of clouds and precipitation constitutes an important observational gap in the global observing system. We present ground-based measurements using a new radar instrument operating near the 183 GHz H₂O line for profiling water vapor inside of planetary-boundary-layer clouds, and develop an error model and inversion algorithm for the profile retrieval. The measurement technique exploits the strong frequency dependence of the radar beam attenuation, or differential absorption, on the low-frequency flank of the water line in conjunction with the radar's ranging capability to acquire range-resolved humidity information. By comparing the measured differential absorption coefficient with a millimeter-wave propagation model, we retrieve humidity profiles with 200 meter resolution and typical statistical uncertainty of 0.6 g/m³ out to around 2 km. **This value for humidity uncertainty corresponds to measurements in the high-SNR limit, and is specific to the frequency band used.** The measured spectral variation of the differential absorption coefficient shows good agreement with the model, **validating supporting** both the measurement method assumptions and the measurement error model. By performing the retrieval analysis on statistically independent data sets corresponding to the same observed scene, we demonstrate the reproducibility of the measurement. An important trade-off inherent to the measurement method between retrieved humidity precision and profile resolution is discussed **using an ensemble of ground-based measurements.**

Copyright statement. ©2018 California Institute of Technology. Government sponsorship acknowledged.

15 1 Introduction

In this work, we discuss the implementation of differential absorption radar (DAR) for measuring humidity profiles inside of boundary-layer clouds (Lebsock et al., 2015; Millán et al., 2016). The DAR method, which is the microwave analog of the mature differential absorption lidar (DIAL) method (Browell et al., 1979), combines the range-resolving capabilities of radar with the strong frequency dependence of atmospheric attenuation near a molecular rotational absorption line to retrieve density profiles of the absorbing gas along the line of sight. Recently, there was a demonstration of microwave integrated path differential absorption in airborne measurements of sea surface air pressure without range resolution (Lawrence et al., 2011), utilizing the 60 GHz O₂ line to measure the total oxygen column. More recently, our group demonstrated a ground-based

DAR for humidity sounding operating between 183 and 193 GHz (Cooper et al., 2018), with primary sensitivity to upper tropospheric water vapor due to significant attenuation in the lower troposphere at these frequencies. That work included a comparison of differential absorption measurements with a millimeter-wave propagation model showing good agreement, and left the topics of error analysis and profile inversion for future investigation. While the 183 to 193 GHz band is attractive for DAR measurements because of the large differential absorption values achievable, transmission at frequencies between 174.8 and 191.8 GHz is prohibited due to reservation for passive-only remote sensing (NTIA, 2015). On the other hand, the 167 to 174.8 GHz band offers fewer transmission restrictions, and features lower absolute absorption, thus enabling penetration into the boundary layer from an airborne or spaceborne platform. Of course, the smaller absolute absorption is accompanied by decreased differential absorption, making the profiling capabilities of this radar coarser than the 183 to 193 GHz DAR. Furthermore, the surface returns in both cloudy and clear-sky areas make possible a DAR measurement of the total water column.

The DAR approach has two unique aspects that complement the weakness of existing methods to remotely sense water vapor. First, because of its ranging capabilities it has precise height registration unlike passive sounding where weighting functions can encompass broad swaths of the atmosphere. Second, in contrast with other methods the DAR signal increases with increasing cloud water content and precipitation. The DAR therefore nicely complements the infrared and microwave sounding techniques, as well as differential absorption and Raman lidar techniques that are commonly used to remotely sense water vapor from the ground (Whiteman et al., 1992; Wulfmeyer and Bösenberg, 1998; Spuler et al., 2015), with a notable airborne DIAL system being the Lidar Atmospheric Sensing Experiment (LASE) (Browell et al., 1998). Importantly, millimeter-wave transparency in clouds allows for airborne or spaceborne measurements of lower tropospheric humidity in cloudy scenes, while DIAL systems typically cannot measure inside boundary-layer clouds due to high optical thickness.

In addition to primary applications in profiling water vapor within clouds, the instrument architecture discussed here represents an important application of recent advances in solid-state G-band technology to meteorological radar. Indeed, there has been lingering interest within the atmospheric remote sensing community for decades in utilizing G-band radar for cloud and precipitation studies, with earlier attempts hampered by limited sensitivity due to available technology (Battaglia et al., 2014). The addition of G-band reflectivity measurements to multi-frequency radar systems, for example a dual-frequency W- and Ka-band system, could provide significantly more information than additional measurements at a lower frequency, because the scattering properties at G-band for typical cloud particle sizes are not of Rayleigh character.

Here we present ground-based measurements using a 167 to 174.8 GHz DAR, provide in-depth measurement error analysis with emphasis on the role of background noise power, and develop a retrieval algorithm based on performing least squares fits of a spectroscopic model to the data. The retrieved profiles constitute the first active remote sensing measurements of water vapor profiles inside of clouds, and open up possibilities for a variety of scientific studies, including investigation of in-cloud humidity heterogeneity and the coupled relationship between boundary-layer clouds and thermodynamic profiles.

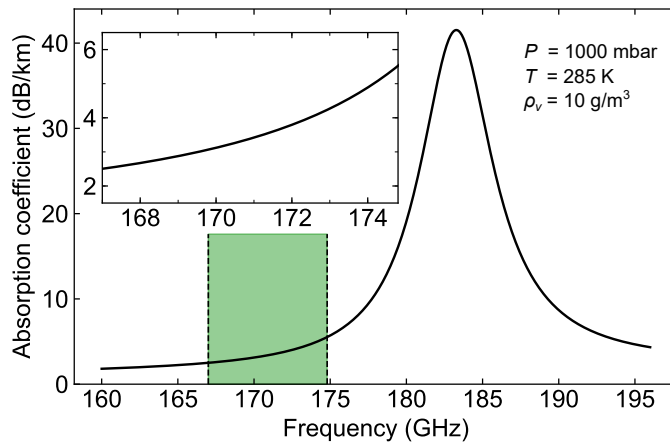


Figure 3. Gaseous absorption coefficient (one-way) calculated using the model from Read et al. (2004) and the parameters listed in the figure. The green shaded region and inset highlight the 167 to 174.8 GHz transmission band for this work.

2 Measurement basis and method

2.1 Differential absorption radar

The DAR technique (Lawrence et al., 2011; Millán et al., 2014; Cooper et al., 2018) utilizes range-resolved radar echoes at multiple carrier frequencies in the vicinity of a gaseous absorption line to probe the frequency-dependent optical depth between two points along the radar line-of-sight. The radar echoes, or returns, may originate from cloud hydrometeors or, in the case of an airborne system, from the Earth’s surface as well, enabling total column optical depth measurements. For closely spaced transmission frequencies near the absorption line center, the hydrometeor scattering properties vary little while the gaseous absorption exhibits strong frequency dependence. By comparing with a known propagation model, these measurements can be employed to retrieve range-resolved density profiles of the absorbing molecule. Furthermore, because of the differential nature of the measurement, one does not require absolute calibration of the radar receiver in order to obtain absolute density values for the absorbing molecule. In the case of a calibrated receiver, both range-resolved density profiles of the absorbing molecule and microphysical properties of the reflecting medium can be retrieved.

Assuming negligible multiple scattering, the radar echo power received from a collection of scatterers filling the beam at a distance r is

$$P_e(r, f) = C(f)Z(r, f)r^{-2}e^{-2\tau(r, f)}, \quad (5)$$

where $C(f)$ includes the frequency dependence of the radar hardware (e.g. transmit power and gain), $Z(r, f)$ is the (unattenuated) reflectivity, and $\tau(r, f)$ is the one-way optical depth including contributions from gaseous and particulate extinction. Taking the ratio of powers for two different ranges r_1 and $r_2 = r_1 + R$ and assuming frequency-independence of the reflectivity

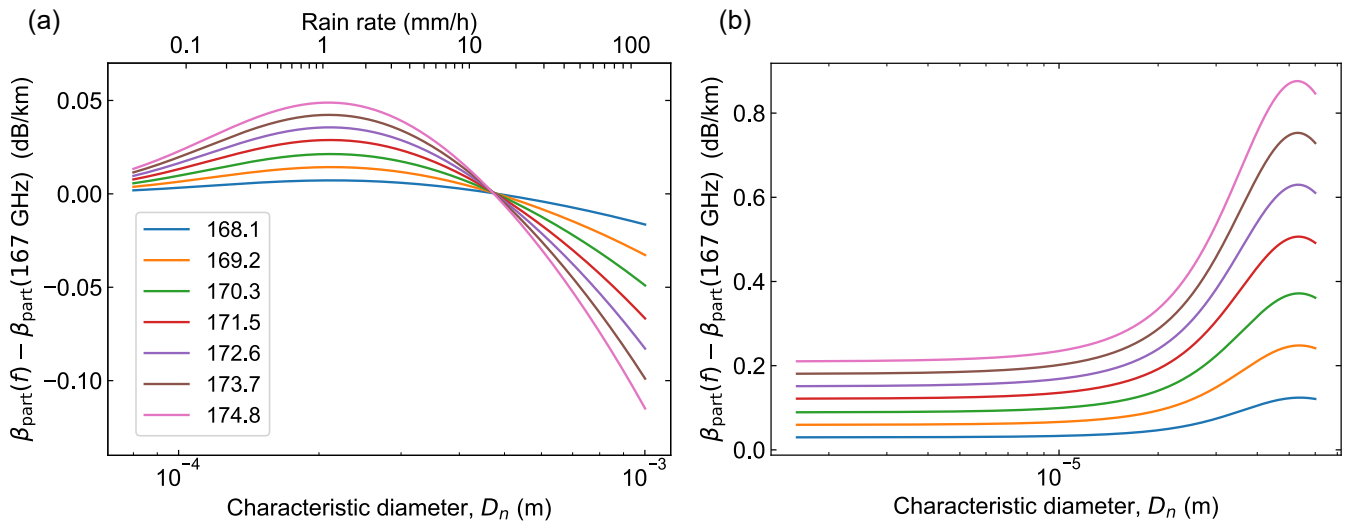


Figure 4. Differential particulate extinction coefficients for (a) rain and (b) cloud. In the case of rain, the DSD characteristic diameter D_n determines the LWC and hence the rain rate, while for clouds we fix $LWC = 500 \text{ mg/m}^3$.

and particulate extinction, we find

$$\frac{P_e(r_2, f)}{P_e(r_1, f)} = \frac{Z(r_2)}{Z(r_1)} \left(\frac{r_1}{r_2} \right)^2 e^{-2\beta(r_1, r_2, f)R}, \quad (6)$$

where

$$\begin{aligned} 5 \quad \beta(r_1, r_2, f) &= \frac{\tau(r_2, f) - \tau(r_1, f)}{R} \\ &= \frac{1}{R} \int_{r_1}^{r_2} \left[\sum_j \rho_j(r) \kappa_j(r, f) + \beta_{\text{part}}(r) \right] dr \end{aligned} \quad (7)$$

is the average absorption coefficient between r_1 and r_2 , $\rho_j(r)$ is the density of the gas component with label j , $\kappa_j(r, f)$ is the corresponding mass extinction cross section, which varies with r due to pressure and temperature, and $\beta_{\text{part}}(r)$ is the particulate extinction coefficient integrated over local drop size distributions (DSDs).

10 Restricting our analysis to millimeter-wave propagation near the 183 GHz water vapor absorption line, the sum over gaseous absorption terms can be replaced by $\rho_v(r) \kappa_v(r, f) + \beta_{\text{gas, bg}}(r)$, where the subscript v corresponds to water vapor and $\beta_{\text{gas, bg}}$ is the background gas absorption coefficient due to all other components, which is assumed to be frequency independent. Assuming that pressure and temperature vary slowly compared to the length scale R , we can therefore write equation (7) as

$$\beta(r_1, r_2, f) = \bar{\rho}_v(r_1, r_2) \kappa_v(f) + \bar{\beta}_{\text{gas, bg}}(r_1, r_2) + \bar{\beta}_{\text{part}}(r_1, r_2), \quad (8)$$

15 where the overbar symbol implies taking the mean value between r_1 and r_2 . Thus, we see that measuring the frequency-dependent contribution to the optical depth between r_1 and r_2 reveals the average water vapor density given the known absorption line shape $\kappa_v(f)$. Figure 3 shows the frequency dependence of the gaseous absorption coefficient $\rho_v \kappa_v(f) + \beta_{\text{gas, bg}}$

in the vicinity of the 183 GHz water vapor line for $P = 1000$ mbar, $T = 285$ K, and $\rho_v = 10$ g/m³. For this work, we utilize the millimeter-wave propagation model from the EOS Microwave Limb Sounder (Read et al., 2004). The 167 to 174.8 GHz transmission band is highlighted in green, as well as shown in the inset to figure 3, revealing a differential absorption coefficient of 3 dB/km for 10 g/m³ of water vapor.

Important to the validity of this DAR method is the dominance of gaseous differential absorption over particulate differential absorption, since we assume that β_{part} is frequency independent. To investigate this for boundary-layer clouds, we perform Mie scattering calculations for liquid spheres and integrate the scattering parameters over DSDs corresponding to clouds and rain for a range of mean diameters. For the DSD, we use a modified gamma distribution of the form

$$N(D) = \frac{N_0}{\Gamma(\nu)} \left(\frac{D}{D_n} \right)^{\nu-1} \frac{1}{D_n} e^{-D/D_n}, \quad (9)$$

where N_0 is a normalization factor with units of particle number per volume that fixes the total liquid water content (LWC), ν is the shape parameter, which is set to 4 for clouds and 1 for rain, and D_n is the characteristic diameter. For rain we enforce an additional constraint that $N_0 = x_1 D_n^{1-x_2}$, where $x_1 = 26.2$ m^{x₂-4} and $x_2 = 1.57$ have been determined in previous studies by comparing to observations (Abel and Boutle, 2012). This allows the entire rain distribution to be determined by the LWC. The rain rate is calculated from this distribution by using the terminal velocity relation from Beard (1976).

The results are shown in figure 4, where we plot the differential particulate extinction, $\Delta\beta_{\text{part}}(f) = \beta_{\text{part}}(f) - \beta_{\text{part}}(f_0)$, as a function of D_n . Here $f_0 = 167$ GHz corresponds to the low-frequency end of the transmission band. In figure 4(a), the corresponding rain rate is displayed on the upper horizontal axis. For the cloud species, the normalization parameter N_0 is not fixed by any additional constraint, and is therefore determined at each D_n to fix the LWC, which is set here to 500 mg/m³. To find the differential particulate extinction for other values of LWC, one can linearly scale the values in figure 4(b). Clearly for precipitation scenarios, the differential extinction from rain is more than two orders of magnitude smaller than that from water vapor. For clouds in the limit of small diameter, the differential particulate extinction asymptotes to the Rayleigh value of $\Delta\beta_{\text{part}}^{\text{Rayleigh}} = 6\pi\text{LWC}\text{Im}(K_w)(f - f_0)/(\rho_w c) = 0.2$ dB/km for $f = 174.8$ GHz, where ρ_w is the density of liquid water, $K_w = (m_w^2 - 1)/(m_w^2 + 2)$, m_w is the complex refractive index of water, and c is the speed of light. For larger values of D_n , the differential extinction is enhanced by a resonant feature characteristic of Mie scattering. Thus, for thick clouds with LWC as large as 500 mg/m³, especially those that contain drizzle drops which tend to lie near this resonant size, there are important bias considerations that warrant future study in order to establish the application of DAR in these particular scenarios. Specifically, to mitigate the potential biases stemming from scattering by hydrometeors, the unattenuated reflectivity can be used to distinguish clouds from precipitation, and the frequency-dependent scattering effects can be modeled and incorporated in the retrieval.

2.2 FMCW radar basics and instrument details

Due to the lower transmit power as compared to conventional radar systems at lower frequencies, the 170 GHz radar is operated in a frequency-modulated continuous-wave (FMCW) mode, which can offer increased sensitivity relative to a pulsed system with the same power because the transmitter is always on. The basic principle of FMCW radar is outlined in figure 5. The transmitted signal is frequency-modulated with a linear chirp waveform of bandwidth ΔF_{chirp} and duration T_{chirp} . After

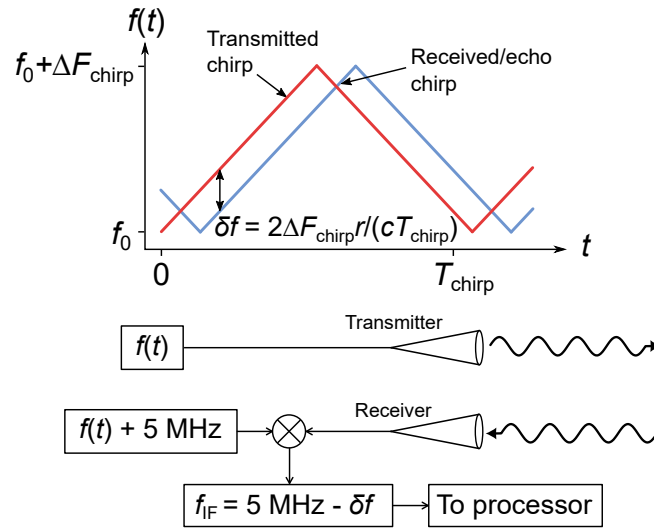


Figure 5. Basic FMCW radar schematic. See Section 2.2 for discussion.

scattering off of a target at a distance r from the radar, the received chirp is delayed in time by an amount $2r/c$, ~~where c is the speed of light~~, leading to a fixed frequency offset of $\delta f = 2\Delta F_{\text{chirp}} r / (cT_{\text{chirp}})$ relative to the transmitted frequency chirp. By downconverting the received signal using the transmitted frequency $f(t)$ shifted by 5 MHz for convenient amplification and detection, the fixed frequency offset between transmitted and received chirps is converted into a constant frequency signal in the intermediate frequency (IF) stage. Signal processing techniques are then used to convert the IF time-domain signal to a range-resolved power spectrum. In the IF power spectrum, the zero-range point is located at 5 MHz and the echo power from a range R is located at $f_{\text{IF}}(r) = 5 \text{ MHz} \pm \delta f(r)$, where the positive(negative) sign applies for decreasing(increasing) frequency chirps.

Our system utilizes state-of-the-art millimeter-wave components designed at the Jet Propulsion Laboratory (JPL) and builds on years of FMCW radar development for security and planetary science applications (Cooper et al., 2011, 2017). The architecture is similar to that presented in an earlier work (Cooper et al., 2018) which demonstrated the DAR technique between 183 and 193 GHz, but modified to transmit in the less restricted 167 to 174.8 GHz band, to perform narrow-bandwidth frequency chirps, and to provide a 5 MHz offset of the zero-range radar signal from zero frequency within the IF band. The IF offset is helpful for future calibrated power measurements because of various effects that inhibit accurate power estimation near zero frequency. The radar has an average transmit power of 140 mW, is outfitted with a 6 cm primary aperture with corresponding gain of 40 dB, and uses a frequency chirp of bandwidth $\Delta F_{\text{chirp}} = 60 \text{ MHz}$ and duration $T_{\text{chirp}} = 1 \text{ ms}$, resulting in a range resolution of $\Delta r = c/2\Delta F_{\text{chirp}} = 2.5 \text{ m}$. **In general, the choice of radar range resolution involves a compromise between acquiring more statistically independent samples within a given target volume to reduce uncertainty for bright targets, and having a longer integration time to reduce noise power and thus increase SNR for weak targets. The choice of 2.5 m allows us to downsample the range dimension by a factor of 11 to realize our desired profile resolution of 27.5 m, with decreased uncertainty for the**

Table 1. Hardware and radar signal acquisition parameters used in this work. The noise figure reported is for a complex radar signal detected using a double-sideband front-end mixer.

Parameter	Value	Unit
Transmit frequency	167 - 174.8	GHz
Transmit power	140	mW
Noise figure	< 8	dB
Primary aperture diameter	6	cm
Antenna gain	39	dB
Far-field beam width (FWHM)	1.9	degrees
Side lobe level	-23	dB
Chirp bandwidth	60	MHz
Chirp time	1	ms
Range resolution	2.5	m

bright clouds measured in this work. ~~Planned future upgrades to the system will include the installation of a 60 cm primary aperture and corresponding 20 dB increase in gain, as well as an increase in transmit power by a factor of 4.~~ A summary of relevant radar hardware parameters is given in table 1.

5 To process the downconverted radar signal, we first sample it using an analog-to-digital converter (ADC) with a sampling frequency of 20 MHz for the 1 ms duration of the chirp. Then we apply a Hanning window in the time domain before performing a fast Fourier transform (FFT) to obtain the range-resolved power spectrum. Application of the Hanning window reduces side-lobes from bright targets as well as the large transmit/receive leakage signal that is always present at zero-range. For the radar parameters listed above, the corresponding conversion factor from IF frequency to target range is $\delta f(r)/r = 400$ kHz/km.

10 2.3 Power measurement uncertainty

The starting point for assessing the achievable precision in humidity using DAR measurements is the statistical uncertainty of the radar power measurements themselves. Until this point, we have ignored the role of background noise power in the radar spectrum, which is an important factor in any realistic receiver. In general, the noise power within a given radar range bin P_n is proportional to the sum of the receiver noise temperature and the antenna temperature, which itself is proportional to the scene brightness temperature. By considering the simultaneous coherent detection of noise (P_n) and radar echo (P_e) power, one can show that the statistical uncertainty of the *detected* power, $P_d = P_e + P_n$, is given by (see Appendix A)

$$\sigma_d = \frac{1}{\sqrt{N_p}} (P_e^2 + 2P_e P_n + P_n^2)^{1/2}, \quad (10)$$

where N_p is the number of radar pulses transmitted.

In order to accurately determine the frequency dependent optical depth between two range bins, it is critical to obtain a separate measurement of the background noise power in the absence of radar echoes and subtract this off of P_d . To see why

this is, consider equation (6) with the left hand side replaced by $P_d(r_2, f)/P_d(r_1, f)$, which is equivalent to interpreting the detected power as the true echo power, set $Z(r_2) = Z(r_1)$ for simplicity, and consider the limit $P_e \ll P_n$ (i.e. $P_d \rightarrow P_n$). In this case we would find that $\exp(-2\beta(r_1, r_2, f)R) \rightarrow 1$ regardless of the actual value of P_e , and thus would incorrectly estimate a vanishing water vapor density, when in fact it is the echo power which has vanished. Similarly, for modest values of the signal-to-noise ratio $\text{SNR} \equiv P_e/P_n$, this would lead to a systematic underestimate of the true humidity. Therefore, after subtracting the separate noise power measurement from P_d we obtain a measurement of P_e with total uncertainty $\sigma_e = (\sigma_d^2 + \sigma_n^2)^{1/2}$, where $\sigma_n = P_n/\sqrt{N_p}$ is the noise power measurement uncertainty (see equation (10) with $P_e = 0$). The relative uncertainty in the measured echo power is therefore

$$10 \quad \frac{\sigma_e}{P_e} = \frac{1}{\sqrt{N_p}} \left(1 + \frac{2}{\text{SNR}} + \frac{2}{\text{SNR}^2} \right)^{1/2}. \quad (11)$$

As will be discussed in Section 3, the range dimension is purposefully oversampled in our measurements, allowing us to decrease the statistical power uncertainty at a given range by averaging N_b adjacent range bins. The resulting relative power uncertainty is given by

$$\frac{\sigma_e}{P_e} = \frac{\xi(N_b)}{\sqrt{N_p N_b}} \left(1 + \frac{2}{\text{SNR}} + \frac{2}{\text{SNR}^2} \right)^{1/2}, \quad (12)$$

15 where $\xi(N_b) \geq 1$ is a factor of order unity accounting for covariances between adjacent range bins that arise due to applying a window function to the time-domain radar signal before transforming to Fourier space. For the Hanning window used in this work, this function is given by $\xi(N_b) = \left(1 + \frac{N_b-1}{N_b} \frac{8}{9} \right)^{1/2}$.

2.4 Inversion algorithm for profile retrieval

Under the simplifying assumptions introduced in the Section 2.1, and assuming that pressure and temperature are known as a function of range, the inverse problem to retrieve humidity can be solved directly. The implications of the latter assumption are explored in Appendix C. To invert the radar spectra, we consider a set of measured echo powers $P_e(r_i, f_j)$ for ranges $\{r_1, r_2, \dots, r_m\}$ and transmission frequencies $\{f_1, f_2, \dots, f_{N_f}\}$, where $r_{i+1} - r_i = \Delta r$ is the radar range resolution. We note that in most circumstances we employ a retrieval step size R that is larger than Δr , since, as we'll show below, the precision in our retrieved humidity scales favorably with total optical depth and hence with increasing R . Then, given a step size such that 25 $R = r_{i+S} - r_i$ for some integer S , we form the frequency-dependent measured quantity

$$\gamma_i(f_j) = -\frac{1}{2R} \ln \left[\left(\frac{r_{i+S}}{r_i} \right)^2 \frac{P_e(r_{i+S}, f_j)}{P_e(r_i, f_j)} \right] \quad (13)$$

for each starting range r_i . From equation (6), we see that we can extract the average humidity between r_i and r_{i+S} by performing a least squares fit of the function

$$\hat{\gamma}(f) = \bar{\rho} \kappa_v(f) + B \quad (14)$$

to the measurements for each i , where B is a frequency-independent offset containing information about dry air gaseous absorption, particulate extinction, and the relative reflectivity of the two ranges in question. We drop the v subscript on the water vapor density in the above equation for simplicity of notation. The resulting humidity estimates $\{\bar{\rho}_1, \bar{\rho}_2, \dots, \bar{\rho}_{m-S}\}$ have a corresponding range axis $\{\bar{r}_1, \bar{r}_2, \dots, \bar{r}_{m-S}\}$ where $\bar{r}_i = (r_i + r_{i+S})/2$, and have associated uncertainties determined from the fitting procedure.

Using standard error propagation, the estimated uncertainty in the measured quantity $\gamma_i(f_j)$ defined in equation (13) is

$$\sigma_{\gamma_i}(f_j) = \frac{1}{2R} \left[\left(\left. \frac{\sigma_e}{P_e} \right|_{r_{i+S}, f_j} \right)^2 + \left(\left. \frac{\sigma_e}{P_e} \right|_{r_i, f_j} \right)^2 \right]^{1/2}. \quad (15)$$

In order to derive a simple analytical expression for the relative uncertainty in the retrieved humidity, we restrict ourselves for the moment to considering two transmission frequencies, f_1 and f_2 . In this case, we can combine equations (6), (8), and (13) to obtain the humidity directly,

$$\bar{\rho}(\bar{r}_i) = [\kappa_v(f_2) - \kappa_v(f_1)]^{-1} [\gamma_i(f_2) - \gamma_i(f_1)], \quad (16)$$

with the associated relative uncertainty

$$\left. \frac{\sigma_{\bar{\rho}}}{\bar{\rho}} \right|_{\bar{r}_i} = \frac{1}{2\Delta\tau} \left[\sum_{j=1,2} \left(\left(\left. \frac{\sigma_e}{P_e} \right|_{r_{i+S}, f_j} \right)^2 + \left(\left. \frac{\sigma_e}{P_e} \right|_{r_i, f_j} \right)^2 \right) \right]^{1/2}, \quad (17)$$

where $\Delta\tau = [\kappa_v(f_2) - \kappa_v(f_1)]\bar{\rho}(\bar{r}_i)R$ is the differential optical depth for f_1 and f_2 between range bins r_i and r_{i+S} . Equation (17) reveals that there are three linked quantities determining the sensitivity of the system: (1) the magnitude of the DAR signal quantified by $\Delta\tau$, (2) the statistical uncertainty of the power measurements given by the quadrature sum of relative errors in equation (17), and (3) the relative uncertainty in the derived value for the humidity. Thus, given a set of measured echo powers and a specific value for the humidity, there is a trade-off between spatial resolution of the retrieval and relative uncertainty in the humidity estimate. These ideas will be explored in Section ??.

An important and subtle point regarding the uncertainty in the measured quantity $\gamma_i(f_j)$ is that equation (15) relies on a Taylor expansion in the relative error σ_e/P_e , and therefore is only valid for measurements with SNR above some critical value that depends on the number of measurements N_p . Because there is no closed-form expression for the probability distribution function (PDF) of $\gamma_i(f_j)$, we resort to a Monte Carlo analysis, which is described in Appendix B, to generate numerically the relevant PDFs for the parameters used in this work. From this analysis, we find that for $N_p = 2000$ pulses and $N_b = 11$ averaged bins, the Taylor expansion method is accurate for measurements with **SNR \gg 0.1 SNR $>$ -10 dB**.

We note here that it is typical of differential absorption systems to utilize only two frequencies: one on-line, and one off-line. However, in this work we are concerned with validating both the spectroscopic model used and the radar hardware itself, which could be subject to unknown frequency-dependent systematic effects. The regression approach discussed above thus provides for a robust comparison of the measured frequency dependence $\gamma_i(f_j)$ with the model $\hat{\gamma}(f)$, while a two-frequency approach would mask inconsistencies between measurements and model, or systematic hardware effects, since the two free parameters $\bar{\rho}$

and B are fully determined given two frequency points. Furthermore, a distributed set of frequencies allows for the possibility of extending retrievals deeper in range for moist atmospheres, as frequencies closer to the line center will be attenuated more strongly, and can be excluded from the fits described above when the critical SNR value is reached.

5 3 Boundary-layer measurements and analysis

3.1 Radar characteristics, spectra, and filtering

In this section we report on measurements performed at JPL on March 15, 2018 using the proof-of-concept differential absorption radar described in Section 2.2. For these measurements, we implement a new signal processing technique for real-time noise floor characterization, utilizing a triangle-wave frequency chirp (i.e. bidirectional) instead of a sawtooth-wave (i.e. uni-
 10 directional). According to FMCW radar principles, the echo spectrum switches from residing on the low to the high-frequency side of the zero-range signal (i.e. 5 MHz) for increasing and decreasing linear frequency chirps, respectively. As shown in figure 6(a), this fast switching of the chirp direction alternately exposes the noise floor on each side of the zero-range point within the IF band, and provides accurate and nearly continuous estimation of the system noise power and the passive signal corresponding to the scene brightness temperature at each frequency bin. This technique is especially advantageous for
 15 airborne/spaceborne applications, as the brightness temperature of the observed scene can change on fast timescales due to different surface types (e.g. ocean vs. land) and from the presence or absence of clouds.

Figure 6 showcases a few aspects of a single ground-based DAR measurement, for which the conditions were light drizzle and a cloud located a few hundred meters off the ground. For all the field measurements discussed in this work, we acquire $N_p = 2000$ pulses for each of 12 frequencies equally spaced between 167 and 174.8 GHz, with the radar positioned just inside
 20 a building, pointing at 30° elevation. The experimental sequence is as follows: first, we perform 40 frequency chirps at a given transmission frequency before switching to another frequency, which takes 1 ms. The received signal is downconverted to baseband, digitized in an analog-to-digital converter (ADC), and processed in real-time as described in Section 2.2. We achieve a system duty cycle of $> 90\%$, resulting in a total measurement/observation time of ≈ 25 seconds.

By subtracting the respective noise floors from the increasing and decreasing frequency chirp measurements (figure 6(a)),
 25 and subsequently combining the mirrored spectra, we obtain our estimate of the echo power spectra. In figure 6(b), we plot the echo power spectra scaled by r^2 for the 12 transmission frequencies before bin averaging, which reveals the range dependence of the quantity $Z(r) \exp(-2\tau(r, f))$. Each spectrum is normalized to its value at 100 meters. Thus, we observe the differential absorption due to water vapor directly from the spreading of the spectra with increasing range, where for a particular range, the plotted values increase monotonically with decreasing transmit frequency. After averaging the quantity $r_i^2 P_e(r_i, f_j)$ within a
 30 swath of size $N_b = 11$, we filter the spectra based on the Monte Carlo analysis in Appendix B, keeping only those points with **SNR > 0.1 SNR > -10 dB**, and are left with the smoothed profiles shown in figure 6(c). Figure 6(d) shows the relative error in the binned ($N_b = 11$) echo power measurement (blue circles) plotted against the measured SNR for all 12 frequencies. The measured values agree very well with those predicted by equation (12) (black dashed line), indicating that our statistical model based on speckle noise, which underlies the Monte Carlo simulations implemented in this work, is accurate.

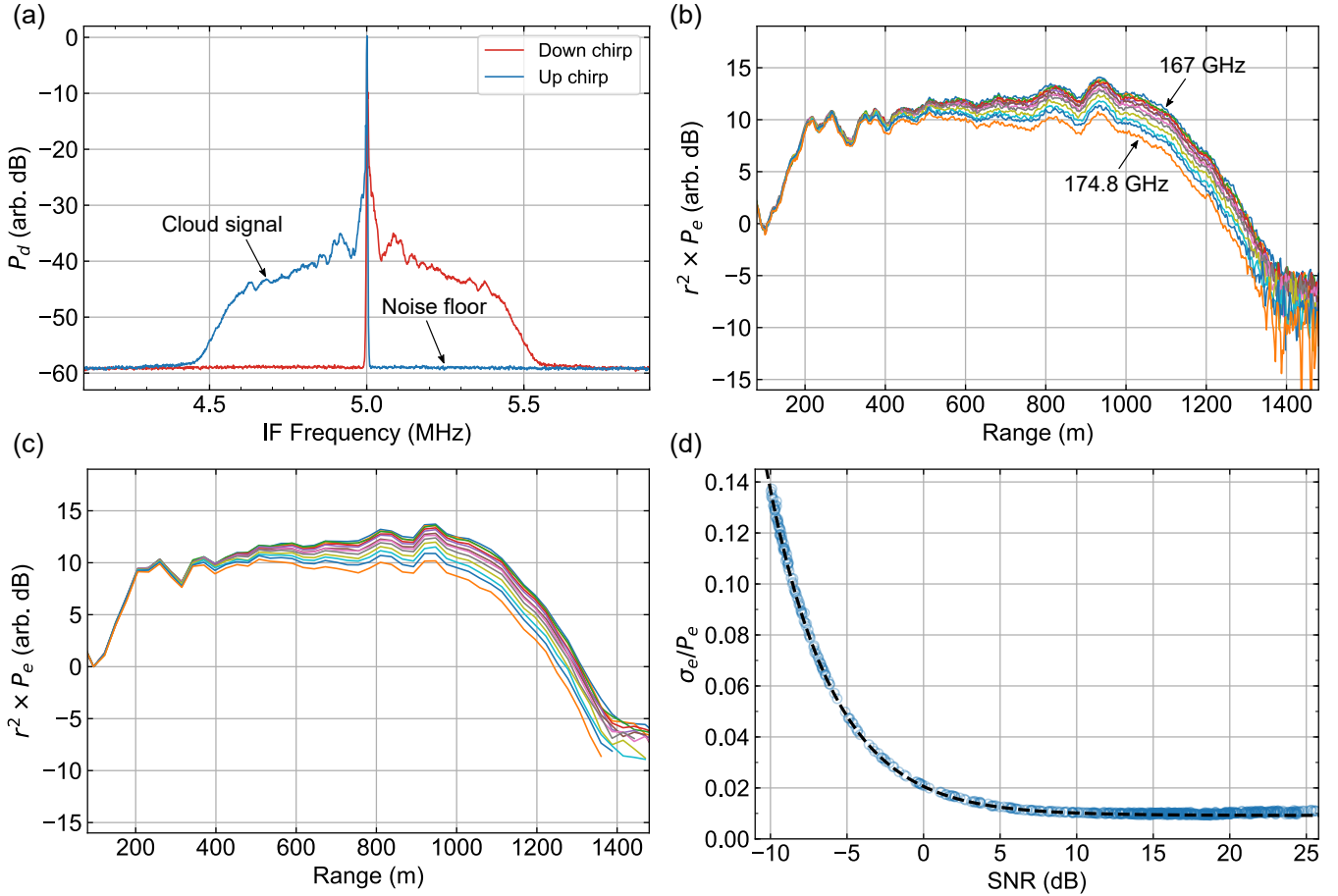


Figure 6. DAR measurement spectra. (a) The bidirectional frequency chirp technique provides for accurate, real-time characterization of the background noise floor within the radar’s IF band, with no loss of measurement duty cycle. Here the detected power spectrum for $f_j = 167$ GHz is shown. The IF frequency to range conversion factor is 400 kHz/km. (b) Echo power spectra normalized to their value at 100 m for the 12 transmission frequencies. The large variability in the signals near 1.4 km indicates the system reaching the noise floor. (c) Echo power spectra after averaging $N_b = 11$ adjacent bins, and filtered for points with $\text{SNR} \geq 0$; $\text{SNR} > -10$ dB. (d) Measurement relative error (blue circles) for all traces in (c) compared with the statistical model (equation (12), dashed black line).

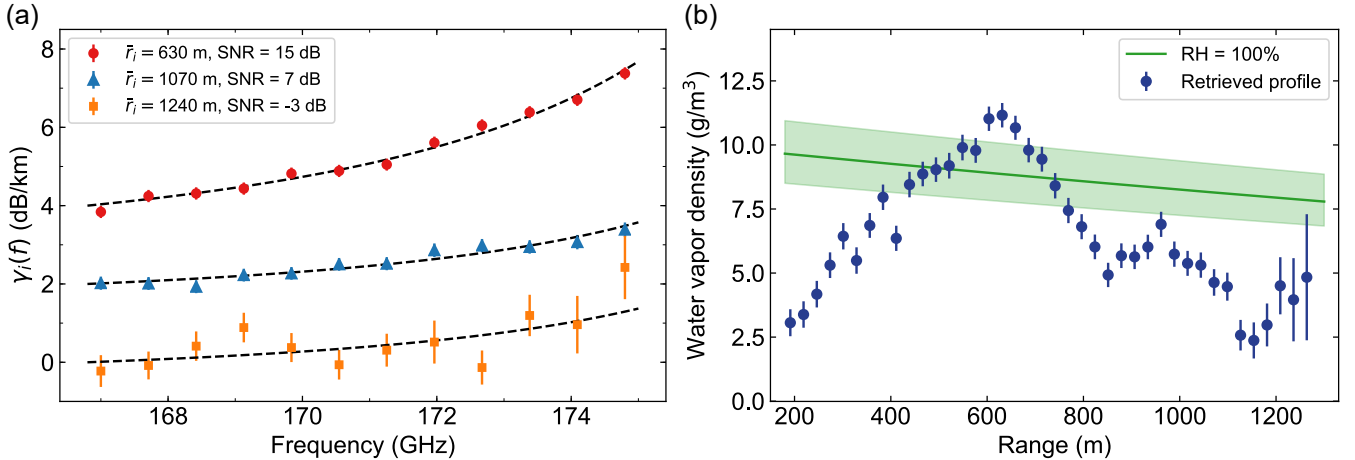


Figure 7. Water vapor profile retrieval for DAR spectra from figure 6. (a) Three examples of least-squares fits of the millimeter-wave propagation model to DAR measurements. Artificial offsets are imposed in order to plot all three on the same graph. (b) The retrieved profile exhibits roughly constant absolute humidity error until $\text{SNR} \approx 10$ dB (1 km). See Sections 2.4 and 3.2 for retrieval details. The green line shows the saturated water vapor density range dependence using a near-surface temperature of 11°C and lapse rate of $6^\circ\text{C}/\text{km}$. The shaded regions correspond to deviations of $\pm 2^\circ\text{C}$.

3.2 Water vapor profile retrieval

Using the averaged, filtered spectra in figure 6(c), we proceed towards retrieving the water vapor density profile using the procedure outlined in Section 2.4. For the profiles presented in this section, we utilize a retrieval step size of $R = 200$ m. Beginning with an initial range of $r_1 = 100$ m, we form the 12 quantities $\gamma_i(f_j)$ for each starting r_i in the set $\{r_1, r_2, \dots, r_{m-S}\}$, and perform a least-squares fit of the function $\hat{\gamma}(f)$ to the data at each range point. Note that the retrieved water vapor density $\bar{\rho}_i$ is related only to the difference between the value of the fitted function at 174.8 and 167 GHz, while the offset is related to particulate extinction and hydrometeor reflectivity, and is disregarded in this work. The pressure and temperature dependence of the absorption line shape is included in the fitting model using reported values at the surface from a nearby weather station, and assuming an exponential pressure profile with a scale height of 7.5 km and a temperature lapse rate of $6^\circ\text{C}/\text{km}$. We note that for the relatively short vertical extents of the profiles from these ground measurements (e.g. $1.4 \sin 30^\circ$ km for figures 6 and 7), the retrieved $\bar{\rho}$ values are quite insensitive to the assumed thermodynamic profiles (see Appendix C).

An important element of the DAR technique in general is utilizing an accurate model for the absorption line shape. Examples of line shape fits to the data are shown in figure 7(a) for three different values of SNR, with arbitrary offsets imposed on the three traces to permit simultaneous plotting. To assign SNR values to these points, we compute the mean SNR for the 12 frequencies at r_i and r_{i+S} , and use the smaller of the two. Clearly the millimeter-wave model accurately captures the frequency dependence of the measurements, which is supported quantitatively by the typical reduced-chi-square values of $\chi_{\text{red}}^2 \approx 1$ for these fits. The retrieved water vapor density profile is shown in figure 7(b), where the range \bar{r}_i assigned to each fitted value $\bar{\rho}_i$ is the midpoint

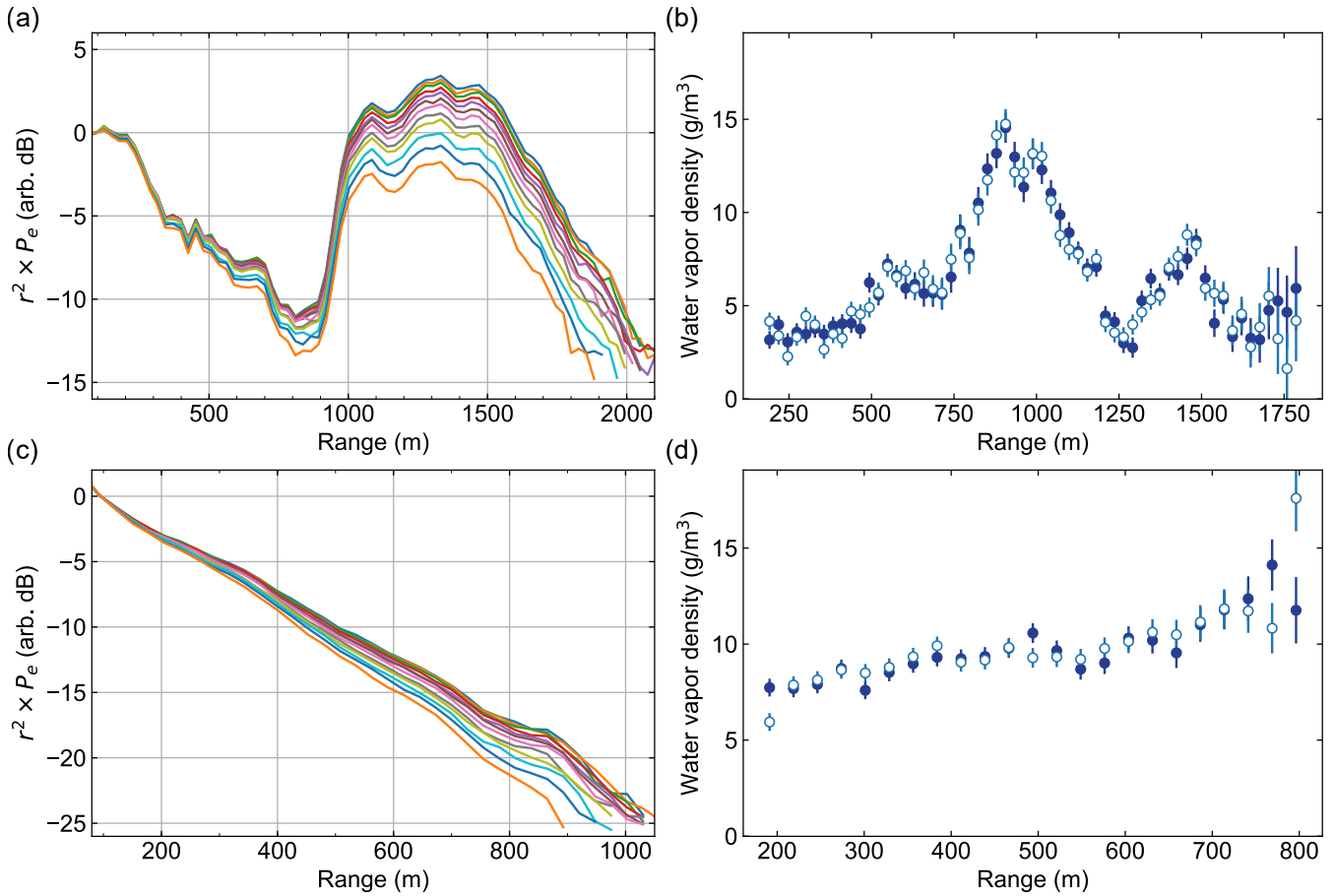


Figure 8. Retrievals for different cloud and precipitation conditions. (a) Averaged DAR power spectra ($N_b = 11$) for light rain near the surface, with a cloud extending from 1 to 2 km. (b) Retrieved humidity profiles for two independent data sets corresponding to the same scene from (a). (c) Averaged DAR power spectra ($N_b = 11$) for heavy precipitation near the surface with strong particulate extinction. (d) Independent retrievals from two data sets for scene in (c).

of r_i and r_{i+S} . Also plotted here is an estimate of the saturation vapor density given our lapse rate assumption. This profile is consistent with a cloud base between 400-600 meters and shows qualitatively good agreement with the expectation that the relative humidity is approximately 100% in liquid cloud layers. Note that because the retrieved values correspond to the mean humidity between r_i and r_{i+S} , we effectively retrieve the profile convolved with a box of size R (200 m here). For this retrieval, the absolute humidity errors lie between 0.55 and 0.60 g/m³ until around 1 km (~~SNR \approx 10~~ SNR \approx 10 dB), where the error steadily increases until the final retrieval point at 1.25 km with $\sigma_{\bar{\rho}} = 2.9$ g/m³. The value of $\sigma_{\bar{\rho}}$ in the high-SNR regime (i.e. the first 1 km) remains roughly constant, even though $\bar{\rho}$ varies by a factor of 3, since the absolute humidity error is independent of the humidity itself, and depends only on the differential mass extinction cross section $\kappa_v(174.8 \text{ GHz}) - \kappa_v(167 \text{ GHz})$, the retrieval step size R , and the power measurement uncertainty (see equation (17)).

Though we do not have independent, coincident water vapor profile measurements with which to validate the accuracy of the retrieval, we can investigate repeatability and consistency of this DAR method by performing the retrieval on coincident, independent DAR measurements of the same exact scene. To do so, we acquire $N_p = 4000$ pulses at each frequency with a total measurement time of 50 seconds, and parse the data into two groups of $N_p = 2000$ pulses both spanning the full 50 seconds. The results are shown in figure 8, where we also present measurements of different cloud and precipitation scenarios than that presented in figures 6 and 7. In figure 8, (a) and (b) correspond to light rain at the surface with a cloud boundary at 1 km range, and (c) and (d) to heavy rain at the surface with strong particulate extinction. The retrievals from the two independent sample sets in both cases agree quite well, which showcases the reproducibility of the measurement and indicates that the estimated humidity error accurately captures the sample scatter.

Given a measured range-resolved echo power spectrum, what retrieval range resolution can we achieve for a specified minimum retrieval precision? As discussed briefly in Section 2.4, the relative error in the retrieved humidity $\sigma_{\bar{\rho}}/\bar{\rho}$ (see equation 17) for a given power measurement uncertainty varies inversely with the differential optical depth, and thus depends on both the retrieval step size R (i.e. retrieval resolution) used *and* the absolute value of the humidity $\bar{\rho}$. Alternatively, one can look at the absolute error and rearrange equation 17 to find that, for a given pair of frequencies and power measurements at two ranges, the product of $\sigma_{\bar{\rho}}$ and R is constant. Hence, reducing the retrieval step size by some factor increases the absolute humidity error by the same factor. In future work we will implement a retrieval algorithm that has adaptive range resolution based on both the inherent signal (i.e. humidity) and the measurement noise.

4 Conclusions

A proof-of-concept humidity-profiling DAR operating between 167 and 174.8 GHz has been constructed and tested from the ground. The instrument builds on progress made in an earlier version operating between 183 and 193 GHz (Cooper et al., 2018), and employs a new signal processing technique for performing real-time noise power spectrum characterization and subtraction, providing for higher accuracy measurements of the radar echo power. A new direct inversion algorithm for retrieving humidity based on least squares fits to a spectroscopic model is applied to the measured echo power spectra, showing close agreement between the measurement and model frequency dependence. The humidity profiles retrieved from two statistically

independent measurement sets of the exact same scene are in close agreement, highlighting the reproducibility of the method. The uncertainties in the power measurements, which in part determine the retrieved humidity uncertainty, agree very well with a statistical model based on radar speckle noise that incorporates the effects of background noise subtraction and down sampling, or binning, of the measured spectra.

Development of an operational airborne 167-174.8 GHz DAR is currently in progress, which will include an additional 20 dB of antenna gain and a factor of 4 increase in transmit power. Important future steps for this instrument include validation of the measurement accuracy using coincident measurements of humidity, pressure, and temperature (e.g. from radiosondes), and eventually testing from an airborne platform. Specifically, the surface returns while measuring from an airborne platform will be investigated for retrieval of total column water within the boundary layer. A more significant augmentation of the system could include the addition of passive radiometric channels near the 183 GHz line. This would allow for continuous measurement of vertical humidity profiles when transitioning between clear sky and cloudy areas, and opens the possibility to study biases in the humidity retrieved from radiometric measurements that are caused by scattering and emission from clouds.

Appendix A: Error in detected power

In this appendix, we derive the expression for the detected power uncertainty within a single radar range bin in the presence of background noise (equation (10)). To do so, we begin by assuming that all targets within the scattering volume are randomly distributed, leading to the well-known Rayleigh fading model for the received echo signal (Ulaby et al., 1982). In the context of FMCW radar, we then consider the received complex electric field amplitude E_i corresponding to the i^{th} frequency bin in the FFT spectrum, where we only consider the polarization direction that couples into the radar receiver. Within the Rayleigh fading model, it is shown that for $E_i = E_{0,i}e^{i\phi_i}$, the modulus of the field amplitude $E_{0,i}$ is normally distributed with zero mean and standard deviation σ_E , and the phase ϕ_i is uniformly distributed over the interval $[0, 2\pi]$. Alternatively, we can write the corresponding voltage in the receiver as $V_{e,i} = a_i + ib_i$, where a_i and b_i are uncorrelated and are both normally distributed with zero mean. Then, from the expression converting electric field to power, $P_{e,i} = |V_{e,i}|^2 = \alpha|E_i|^2$, we find the probability distribution function for the received echo power

$$p(P_{e,i} \geq 0) = \frac{1}{\langle P_{e,i} \rangle} e^{-P_{e,i}/\langle P_{e,i} \rangle}, \quad (\text{A1})$$

where the mean equals the variance and is given by $\langle P_{e,i} \rangle = 2\alpha\sigma_E^2$, α is a field-to-voltage conversion factor for the radar, and $p(P_{e,i} < 0) = 0$. Furthermore, we find that $\langle a_i^2 \rangle = \langle b_i^2 \rangle = \langle P_{e,i} \rangle/2$. Though not proven here, the Rayleigh fading model also shows that the expectation value of the received power from N randomly distributed targets is the sum of the expectation values of the individual target echo powers.

Similarly, one can show that Gaussian white noise in the radar signal, which comes from both the scene brightness temperature and the radar electronics, results in a noise voltage within the i^{th} frequency bin of the FFT spectrum with Fourier coefficient $V_{n,i} = c_i + id_i$, where $\langle c_i \rangle = \langle d_i \rangle = 0$ and $\langle c_i^2 \rangle = \langle d_i^2 \rangle = \langle P_{n,i} \rangle/2$. We proceed towards deriving equation (10) by considering the coherent detection of both the radar echo and noise signals. In this case, the detected voltage signal in the

Fourier domain within the i^{th} range bin is $V_{d,i} = V_{e,i} + V_{n,i}$, and the detected power is $P_{d,i} = |V_{d,i}|^2$. Using the expectation values listed above, it is easy to show that

$$\langle P_{d,i} \rangle = \langle P_{e,i} \rangle + \langle P_{n,i} \rangle \quad (\text{A2})$$

5 and

$$\text{Var}(P_{d,i}) = (\langle P_{e,i} \rangle + \langle P_{n,i} \rangle)^2. \quad (\text{A3})$$

Therefore, we recover equation (10) by computing the standard error for N independent measurements, $\sigma_{d,i}^2 = \text{Var}(P_{d,i})/N$.

Appendix B: Monte Carlo Analysis

As discussed in Section 2.3, subtracting off the noise power contribution to the detected power P_d is critical for accurate
 10 humidity estimation. However, for low values of SNR, we clearly expect the result $\langle P_e \rangle = \langle P_d \rangle - \langle P_n \rangle$ to be negative some of
 the time due to finite sampling, where “ $\langle \cdot \cdot \cdot \rangle$ ” denotes the sample average. This is non-physical. Therefore, in order to account
 for these finite sampling effects and the potential breakdown of standard error propagation when σ_e/P_e is not small, we
 employ a Monte Carlo simulation of the DAR measurement. The PDF for the echo power received from randomly distributed
 hydrometeor targets within a single range bin is given by equation A1. In order to generate random samples of the radar
 15 spectrum for transmission frequency f_j , we begin with an idealized spectrum $\langle P_e(r_i, f_j) \rangle$ for which we set $C(f) = Z(r, f) = 1$
 and $\rho_v(r) = \text{constant}$, and sample the distribution (equation (A1)) at each range bin r_i . We then perform a fast Fourier transform
 (FFT) to obtain the corresponding time-domain radar signal, add the effects of background noise using Gaussian white noise,
 and apply a Hanning window. Taking the inverse FFT thus supplies a single random realization of a measured P_d spectrum.
 For the simulated spectra used in this work, we generate $N_p = 2000$ radar pulses with range resolution $\Delta r = 2.5$ m and
 20 average them to realize a single radar measurement. These values for N_p and Δr are the same parameters utilized in the
 field measurements presented in Section 3. We generate 10,000 averaged spectra for both P_d and P_n , giving 10,000 random
 realizations of the echo power measurement. For these simulations, we use $f_j = 167$ GHz and $\rho_v = 7.4$ g/m³.

Our aim is to utilize the Monte Carlo simulations to inform where the Taylor expansion method for error propagation breaks
 down in our estimation of $\sigma_{\gamma_i}(f_j)$, and thus provide a criterion for filtering our measurements. To do so, we fix $N_b = 11$ and
 25 the step size $S = 10$ (i.e. 275 meters) and compute the mean and standard deviation of the Monte Carlo probability distribution
 for the two-way transmission between r_i and r_{i+S} for each r_i . Figure B1 shows the results, where we plot the Monte Carlo
 mean value divided by the *a priori* two-way transmission used to generate the Monte Carlo results, as a function of the
 SNR at r_{i+S} . The solid green lines represent the SNR-dependent errors predicted from equation (12). There are two notable
 deviations that arise for SNR values below 0.1: (1) The error estimated using the standard error propagation formalism begins
 30 underestimating the true standard deviation calculated using the Monte Carlo ensemble, and (2) the mean of the Monte-Carlo-
 generated distribution systematically overestimates the true two-way transmission. We note here that this point of departure
 between the naive error propagation estimate and that from the Monte Carlo distributions does not depend on N_b or S , but is

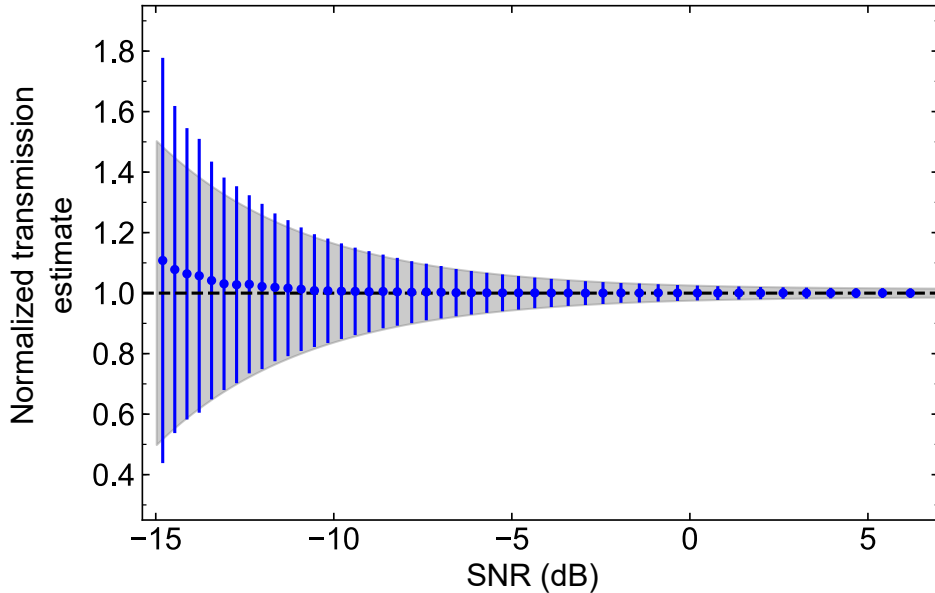


Figure B1. Statistics of low-SNR estimation of two-way transmission. The blue data points represent the means and standard deviations of the Monte Carlo probability distributions, while the green lines represent the error calculated using equation (12). For $\text{SNR} < -10$ dB, the systematic bias of the Monte Carlo mean and underestimation of the true error by equation (12) imply that measurements in this region should be disregarded. In order to access lower values of SNR, one must increase the number of pulses N_p for each measurement.

determined by the number of independent pulses N_p used to realize a single radar measurement. From these simulations, we conclude that the standard error propagation model is sufficient for $\text{SNR} > -10$ dB. Therefore, after down sampling the measured spectra with $N_b = 11$, we eliminate all measured values with $\text{SNR} < -10$ dB, as described in Section

5 3.1.

Appendix C: Retrieval dependence on assumed pressure and temperature values

To assess the dependence of the retrieved humidity on temperature and pressure, we will consider again the case of the two-frequency measurement, using transmission frequencies $f_1 = 167$ GHz and $f_2 = 174.8$ GHz. Then, for a given starting range r_i and step size R , we use the measured quantities $\gamma_i(f_1)$ and $\gamma_i(f_2)$ to solve for the mean humidity between the two ranges,

$$10 \quad \bar{\rho}_i = \frac{\gamma_i(f_2) - \gamma_i(f_1)}{\kappa_{\mathbf{v}}(f_2, P, T) - \kappa_{\mathbf{v}}(f_1, P, T)} = \frac{\gamma_i(f_2) - \gamma_i(f_1)}{\Delta\kappa_{\mathbf{v}}(P, T)}, \quad (\text{C1})$$

where we now explicitly write $\kappa_{\mathbf{v}}$ as a function of temperature T and pressure P , and we've defined the differential mass extinction cross section $\Delta\kappa_{\mathbf{v}}(P, T)$ for these two frequencies. Given reference values of $P_0 = 1000$ mbar and $T_0 = 285$ K, and

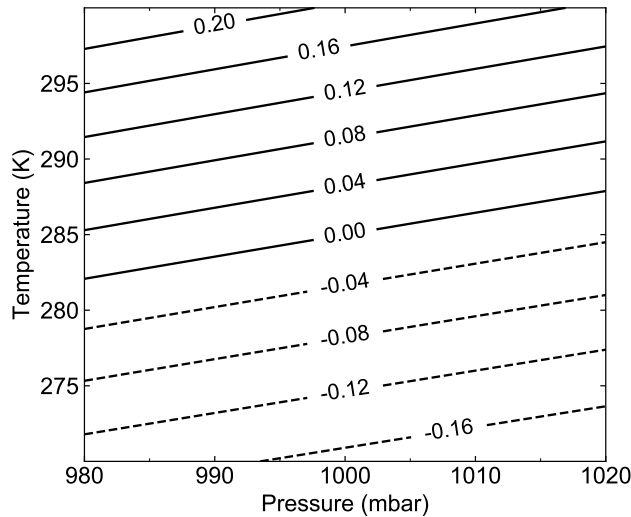


Figure C1. Humidity error for assumed temperature $T_0 = 285$ K and pressure $P_0 = 1000$ mbar versus actual values T and P .

corresponding retrieved humidity $\bar{\rho}_{i,0}$, we calculate the error in our humidity estimate for different conditions P and T as

$$\frac{\bar{\rho}_i - \bar{\rho}_{i,0}}{\bar{\rho}_{i,0}} = \frac{\Delta\kappa_v(P_0, T_0)}{\Delta\kappa_v(P, T)} - 1. \quad (\text{C2})$$

Figure C1 shows the humidity error for pressure deviations of ± 20 mbar and temperature deviations of ± 15 K. Here we see that the retrieved humidity is very weakly dependent on the assumed pressure, and only accrues an error of 10% for a temperature deviation of about 8 K.

Acknowledgements. This research was supported by NASA's Earth Science Technology Office under the Instrument Incubator Program, and was carried out at the Jet Propulsion Laboratory (JPL), California Institute of Technology, Pasadena, CA, USA, under contract with the National Aeronautics and Space Administration. R. Roy's research was supported by an appointment to the NASA Postdoctoral Program at JPL, administered by Universities Space Research Association under contract with NASA.

References

- Manual of Regulations and Procedures for Federal Radio Frequency Management, from the National Telecommunications & Information Administration (NTIA), Revision of the May 2013 Edition, 2015.
- 5 Abel, S. J. and Boutle, I. A.: An improved representation of the raindrop size distribution for single-moment microphysics schemes, *Quarterly Journal of the Royal Meteorological Society*, 138, 2151–2162, 2012.
- Battaglia, A., Westbrook, C. D., Kneifel, S., Kollias, P., Humpage, N., Löhnert, U., Tyynelä, J., and Petty, G. W.: G band atmospheric radars: new frontiers in cloud physics, *Atmospheric Measurement Techniques*, 7, 1527–1546, 2014.
- Beard, K. V.: Terminal Velocity and Shape of Cloud and Precipitation Drops Aloft, *Journal of the Atmospheric Sciences*, 33, 851–864, 1976.
- 10 Browell, E., Ismail, S., and Grant, W.: Differential absorption lidar (DIAL) measurements from air and space, *Applied Physics B*, 67, 399–410, 1998.
- Browell, E. V., Wilkerson, T. D., and McIlrath, T. J.: Water vapor differential absorption lidar development and evaluation, *Appl. Opt.*, 18, 3474–3483, 1979.
- Cooper, K. B., Dengler, R. J., Llombart, N., Thomas, B., Chattopadhyay, G., and Siegel, P. H.: THz Imaging Radar for Standoff Personnel Screening, *IEEE Transactions on Terahertz Science and Technology*, 1, 169–182, 2011.
- Cooper, K. B., Durden, S. L., Cochrane, C. J., Monje, R. R., Dengler, R. J., and Baldi, C.: Using FMCW Doppler Radar to Detect Targets up to the Maximum Unambiguous Range, *IEEE Geoscience and Remote Sensing Letters*, 14, 339–343, 2017.
- Cooper, K. B., Monje, R. R., Millán, L., Lebsock, M., Tanelli, S., Siles, J. V., Lee, C., and Brown, A.: Atmospheric Humidity Sounding Using Differential Absorption Radar Near 183 GHz, *IEEE Geoscience and Remote Sensing Letters*, 15, 163–167, 2018.
- 20 Lawrence, R., Lin, B., Harrah, S., Hu, Y., Hunt, P., and Lipp, C.: Initial flight test results of differential absorption barometric radar for remote sensing of sea surface air pressure, *Journal of Quantitative Spectroscopy and Radiative Transfer*, 112, 247 – 253, international Symposium on Atmospheric Light Scattering and Remote Sensing (ISALSaRS'09), 2011.
- Lebsock, M. D., Suzuki, K., Millán, L. F., and Kalmus, P. M.: The feasibility of water vapor sounding of the cloudy boundary layer using a differential absorption radar technique, *Atmospheric Measurement Techniques*, 8, 3631–3645, 2015.
- 25 Millán, L., Lebsock, M., Livesey, N., Tanelli, S., and Stephens, G.: Differential absorption radar techniques: surface pressure, *Atmospheric Measurement Techniques*, 7, 3959–3970, 2014.
- Millán, L., Lebsock, M., Livesey, N., and Tanelli, S.: Differential absorption radar techniques: water vapor retrievals, *Atmospheric Measurement Techniques*, 9, 2633–2646, 2016.
- Read, W. G., Shippony, Z., and Snyder, W.: EOS MLS forward model algorithm theoretical basis document, Jet Propulsion Laboratory, JPL D-18130/CL#04-2238, Pasadena, CA, USA, 2004.
- 30 Spuler, S. M., Repasky, K. S., Morley, B., Moen, D., Hayman, M., and Nehrir, A. R.: Field-deployable diode-laser-based differential absorption lidar (DIAL) for profiling water vapor, *Atmospheric Measurement Techniques*, 8, 1073–1087, 2015.
- Ulaby, F., Moore, R., and Fung, A.: *Microwave Remote Sensing: Active and Passive*, vol. II, Addison-Wesley Publishing Company, Inc., Reading, Massachusetts, 1982.
- 35 Whiteman, D. N., Melfi, S. H., and Ferrare, R. A.: Raman lidar system for the measurement of water vapor and aerosols in the Earth's atmosphere, *Appl. Opt.*, 31, 3068–3082, 1992.
- Wulfmeyer, V. and Bösenberg, J.: Ground-based differential absorption lidar for water-vapor profiling: assessment of accuracy, resolution, and meteorological applications, *Appl. Opt.*, 37, 3825–3844, 1998.